Low-Speed Unsteady Aerodynamics of a Pitching Straked Wing at High Incidence—Part II: Harmonic Analysis

A. M. Cunningham Jr.*
General Dynamics, Fort Worth, Texas
and
R. G. den Boer†
National Aerospace Laboratory (NLR), Amsterdam, the Netherlands

Part I of this paper described the wind-tunnel model and test program. This part presents data from the test that are amenable to harmonic analysis that limits the amplitudes to about ±4 or ±6 deg but does not limit mean angles or frequencies. Those results are applicable to flutter and dynamic response problems as well as stability and control characteristics at high incidences. Force, pressure, and flow-visualization data are used to describe the perceived flow phenomena and how they interact with the model to produce the aerodynamic forces.

Nomenclature

b	= local wingspan, m
C_m	= wing pitching-moment coefficient, $= m/QSc_r$; reference axis at 73.27% of c_r
C_{m_α}	= slope of C_m wrt α
C_N	= wing normal-force coefficient, N/QS
C_{N_α}	= slope of C_N wrt α
f, $FREQ$	= frequency, Hz
Im( )	= out-of-phase component
$\text{Im}(C_p)_i$	$= \text{Im}(p_i)/Q\Delta\alpha$
i	= SQRT (−1)
k	= see REDFR
m	= mean
Re( )	= in-phase component
$\text{Re}(C_p)_i$	$= \text{Re}(p_i)/Q\Delta\alpha$
y	= spanwise coordinate, m

Introduction

RECENT interest in flying at very high angles of attack beyond the static stall conditions has been kindled by proposals to exploit this flow regime to improve fighter aircraft maneuverability.[1,2] Herbst's concept to fly into the poststall regime to achieve quicker turns[1] and the use of unsteady aerodynamics at high incidence discussed by Lang and Francis[2] open a Pandora's box of new aerodynamic problems. Since these ideas require flying at incidences as high as 90 deg or beyond, a single maneuver could cover attached flows, vortex, and burst vortex flows, as well as totally separated flows. In addition, the more highly separated flows are increasingly sensitive to unsteady and time-history effects; hence, maneuver dynamics become very important under such conditions. An understanding of these flowfields and dynamic effects is needed to design aircraft to exploit the preceding concepts; however, this represents several quantum jumps over current aerodynamic technology.

Aerodynamic loads experienced by flexible maneuvering aircraft may be classified into three distinct categories: 1) quasisteady cruise and maneuvering loads due to rigid-body aircraft motions with static aeroelastic effects, 2) structural dynamic loads due to aircraft vibration as a result of gust response and flutter, and 3) buffet loads due to separated flow fields. In terms of aircraft motions, the first category involves large aircraft attitude excursions, e.g., as in a pitch-up maneuver starting at an incidence of 5 deg and ending at 35 deg. The development of these loads can become very nonlinear, particularly where several flow regimes are traversed during a single continuous maneuver.[3] This development is also sensitive to the maneuver time history such as the starting and stopping angles and angular rates. The second category of structural dynamic loads involves small surface motions, nominally less than 3- or 4-deg incidence change, and high frequencies typical of aircraft natural modes of vibration. These loads are usually linear because of small perturbations; however, the mean flow conditions will directly control how the incremental loads develop for a given surface motion. As an example, aerodynamic loads due to a wing bending mode oscillating at a fixed amplitude are reduced greatly for completely separated flows as compared with attached flows. Finally, the third category of buffet loads does not require aircraft or surface motion to produce the loads, but are influenced by such motions, as has been discussed in Ref. 4.

To understand better the development of aerodynamic loads for fighter aircraft maneuvering beyond stall, a low-speed ($M=0.2$) wind-tunnel test was performed as described in Part I of this paper. A comprehensive data base was developed as a result of this test and was published as an Air Force report[5] with an unlimited distribution. The present paper will present some results and discussions for data from Ref. 5 that are amenable to harmonic analysis. This limits the maximum amplitudes to about ±4 or ±6 deg, but does not limit mean angle or frequency. These results pertain to the second category described earlier for structural dynamic loads and are thus applicable to flutter and dynamic response problems. The results are also meaningful for high-incidence stability and control, but are restricted to small excursions in aircraft attitude about the mean. First, the steady and unsteady characteristics will be discussed to provide a general understanding of the flowfields and related forces and pressures. Next, the first harmonic force data will be analyzed more fully to show the effects of mean angle, frequency, and amplitude. A similar analysis will be presented for the first harmonic pressure data. Finally, flow-visualization results will be presented to illus-

Received Jan. 13, 1988; revision received May 22, 1989.

*Senior Engineering Specialist, Computational Fluid Dynamics Group, Aerospace Technology, Fort Worth Division. Associate Fellow AIAA.

†Research Engineer, Aeroelasticity Department.

trate the harmonic vortex motion during pitch oscillation and to provide further insight into the flowfield characteristics.

Steady Aerodynamic Characteristics

The key to understanding the unsteady aerodynamics is to understand first the steady aerodynamics. The combination of force, pressure, and flow-visualization data available from this test makes it possible to break down the angle-of-attack range of -8 to 50 deg into definable flow regimes separated by smaller transition regimes.

The variations of steady normal force C_N and pitching moment C_m with angle of attack α are shown in Fig. 9 of Part I. Important flowfield characterisitcs and transitions are also denoted where the "sections" referred to in those notations are the pressure transducer rows shown in Fig. 5 of Part I. Corresponding steady pressure data for all four sections are shown in Fig. 1 for $\alpha = 10$, 19, 22.4, 36, and 42.3 deg. The pressure data were chosen to highlight various flow regimes and transitions.

The "linear" range of aerodynamic force development is clearly evident in Fig. 9 of Part I in both the C_N and C_m data from -8 to 8 deg. Beyond 8 deg, the curves show an upward change in slope that is indicative of the development of vortex flows over both the wing and strake. This is illustrated by the pressure data in Fig. 1 at $\alpha = 10$ deg for section 2. The small peak by $2y/b \approx 0.45$ is produced by the strake vortex and the stronger peak at $2y/b \approx 0.8$ by the wing vortex. The vortex structure is also illustrated by the accompanying sketch in Fig. 1.

The vortex flow range continues to develop until $\alpha \approx 18$–19 deg, where a distinct break occurs in both the C_N and C_m data. This break signals the onset of vortex burst, which represents the limit of vortex strength that can be maintained by the flowfields. The burst tends to occur simultaneously for the wing and strake vortices when the two merge, as will be illustrated later with the flow-visualization results. The pressure data for $\alpha = 19$ deg in Fig. 1 show well-developed vortices at both of the forward sections (1 and 2) but a deterioration of pressure recovery on the outboard half of the trailing-edge section (3). The burst vortex structure is also illustrated in the sketch for $\alpha = 19$ deg in Fig. 1.

For increasing α in the burst vortex regime, the strake vortex strength increases but the burst point continues to move forward. These opposing trends result in a much lower slope in the C_N curve, as shown in Fig. 9 of Part I; however, the slope is almost constant from $\alpha = 19$ deg to about 34 deg. The gain in lift forward due to the strake vortex strength increases and the loss in lift aft due to vortex burst forward movement produce a pitch-up in the C_m curve, as shown in Fig. 9 of Part I. The pressure data in Fig. 1 for $\alpha = 19$, 22.4, and 36 deg show the deterioration of the wing vortex strength at section 2 and the continued increase of the strake vortex strength up to 36 deg at section 1. These characteristics are illustrated in the sketches for $\alpha = 19$, 22.4, and 36 deg.

Beyond the maximum value of C_N at $\alpha = 36$ deg, the flow over the entire wing and strake rapidly collapses to completely separated or flat-plate flow. Under these conditions for increasing α, the normal force is falling off and the center of pressure is moving toward the geometric centroid of the planform, as indicated by a rapid decrease in the C_m curve. The pressure data at $\alpha = 42.3$ deg in Fig. 1 show that the pressure distributions are nearly flat at about the same level for all sections except section 1 on the strake. At this angle, the strake vortex burst has progressed forward of section 1, as shown in the sketch for $\alpha = 42.3$ deg.

Another view of how pressure data are related to force data can be obtained by considering only the suction peaks at pressure section 2 associated with the wing and strake vortices plotted vs α, as shown in Fig. 2. The wing vortex peak reaches its maximum strength at about $\alpha = 18$ deg, at which point vortex bursting first appears over the wing, as denoted in Fig. 9 of Part I. The pitch-up in the C_m data corresponds to the loss in lift at the trailing edge, as indicated by the rapid drop in the wing vortex suction peak. Note also that while the wing

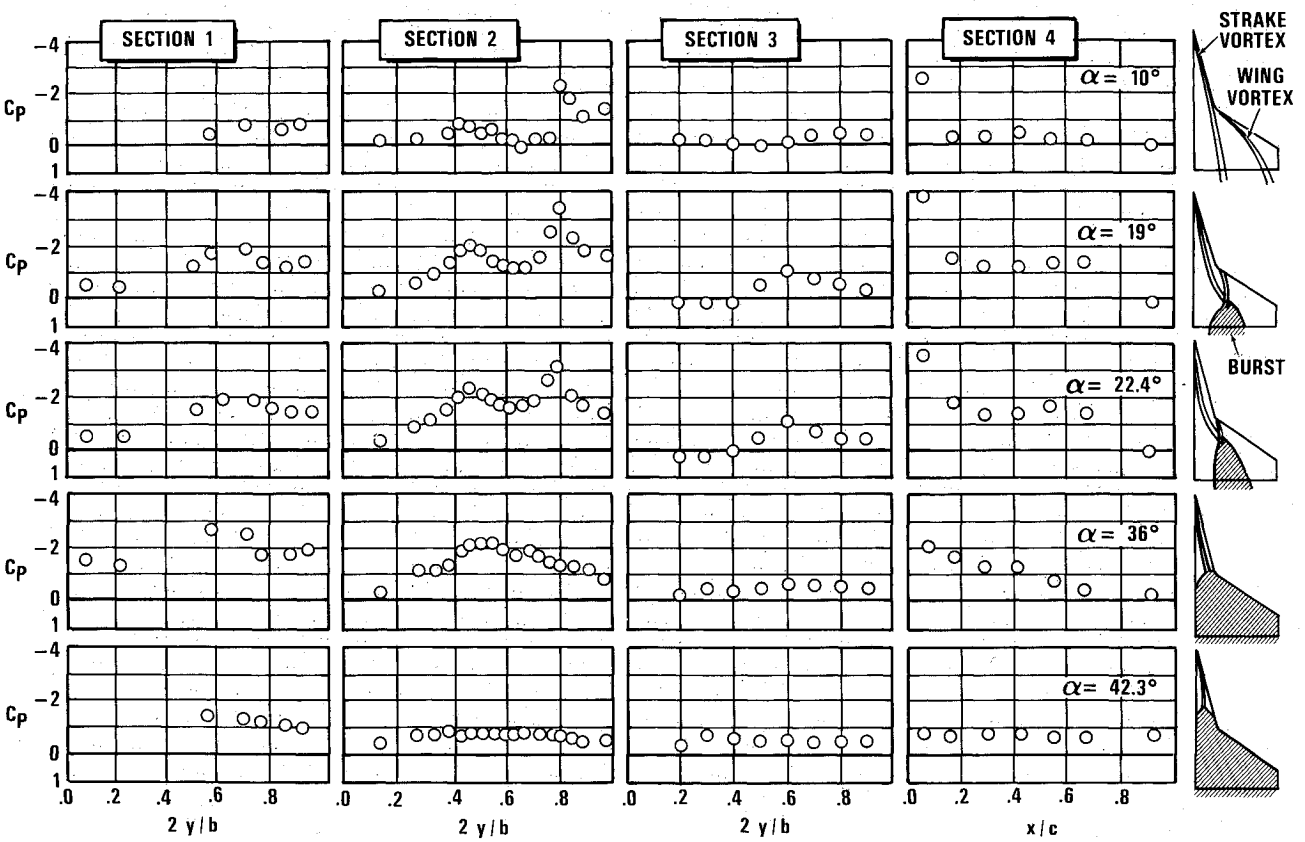

Fig. 1 Steady pressure variation with α.

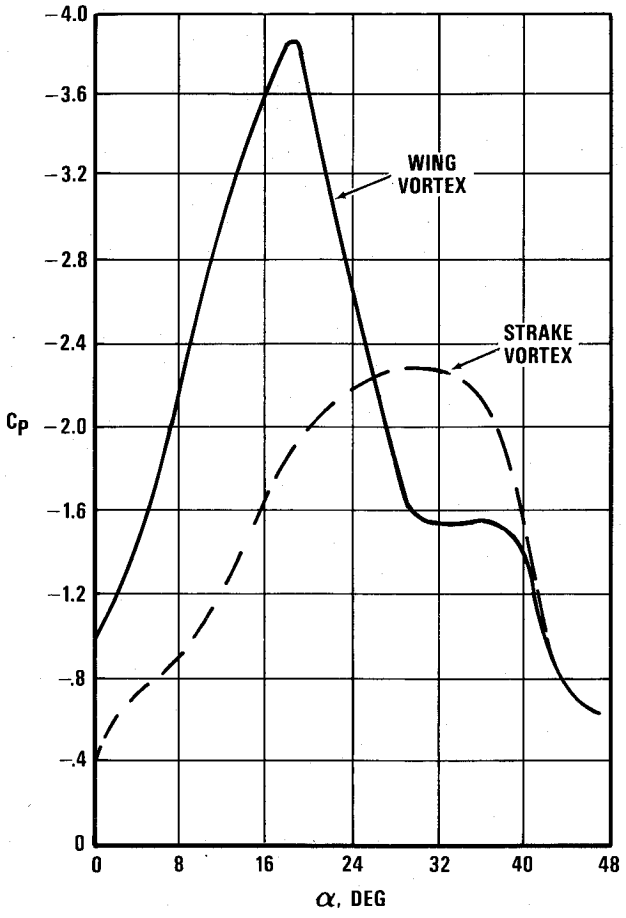

Fig. 2 Vortex suction peak at section 2 as a function of angle of attack.

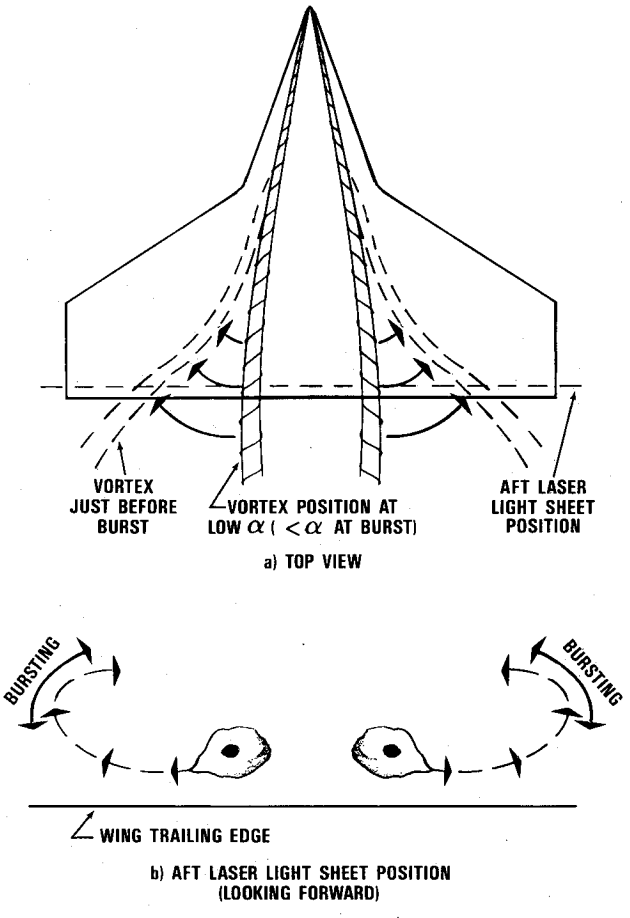

Fig. 3 Sketches of vortex charactristics near burst observed in flow visualization.

peak is falling in Fig. 2, the strake vortex suction peak is rising and continues to do so until about $\alpha = 32$ deg. However, the slope of the strake vortex peak begins to diminish starting at $\alpha = 20$ deg, which correlates with reduction of the C_m curve slope in Fig. 9 of Part I from $\alpha = 22$ to 36 deg near the maximum value of C_N. The wing vortex suction peak shows a flat characteristic from about 31 to 36 deg, which indicates that its burst passed the pressure section 2 at $\alpha = 31$ deg. The rapid fall of the strake vortex suction peak starts at about 36 deg, which corresponds to well-known characteristics of delta wings where burst appears at the trailing edge of a 76-deg delta wing at about 35–38 deg.[6] Maximum C_N occurs at about 36 deg, after which all flows begin to deteriorate rapidly to a fully stalled condition. The strake vortex is still formed, but burst is quickly moving forward, as indicated by the strake vortex suction peak. Fully stalled flow at the section 2 pressure row appers to be reached at about 42–44 deg, where both suction peaks merge.

In addition to the force and pressure data discussed earlier, flow-visualization data provided valuable insight for interpreting the source of changes in the forces and pressures. This was evidenced by the sketches shown in Fig. 1. It was also possible, however, to identify the mechanism that caused the wing and strake vortex bursting. Figure 3a shows sketches of how the strake vortex appeared at low angles and at preburst conditions just before burst, as viewed from the top. The occurrence of the "S"-shaped strake vortex just before burst took place as a final step in a very rapid transition from the straight, low-angle path to the burst condition shown in Fig. 1 for $\alpha = 19$ deg. When viewed from the aft laser-light sheet position (corresponding to pressure section 3, Fig. 5, of Part I) in Fig. 3b, the same transition showed that the strake vortex was wrapping around the wing vortex and bursting as it was lifted away from the wing surface by the wing vortex. Thus, vortex burst for this straked-wing configuration was attributed to the sudden combining of the wing and strake vortices to produce the unstable flow that immediately led to burst vortex flow.

Unsteady Aerodynamic Characteristics

With a better understanding of the various flow regimes for steady flow, the unsteady characteristics will be developed more easily, especially for small-amplitude oscillations. An example of some of the unsteady force data is shown in Fig. 4. These data are the harmonic components of C_{N_α} and C_{m_α} (slopes of C_N and C_m) measured at the model oscillation frequency. The real part is that component which is in phase with model motion, i.e., the value at model maximum angle. The imaginary part is that component which is out of phase with model motion, i.e., the value at the model mean angle of attack with positive pitch rate. Since maximum positive pitch rate leads maximum incidence by a 90-deg phase angle, increasing sensitivity to pitch rate results in an increasing lead angle for the aerodynamic characteristics. In the following discussions, this sensitivity will be referred to as pitch-rate effects and produces a leading phase angle relative to α, whereas phase-lag effects will be a result of aerodynamic lag.

As shown in Fig. 4, the changes in slope closely track the steady data shown in Fig. 9 of Part I over most of the incidence range. This is understandable since the amplitude is only ± 3.5 deg and the frequency is fairly low at 3 Hz ($k = 0.09$). Dominance of the real part at angles up to vortex burst is also expected because the flowfields are well organized. Beyond vortex bursting, however, the imaginary part becomes increasingly important and acturally crosses over at about 36 deg at the occurrence of the maximum value of C_N. This increase of

the imaginary part relative to the real part simply reflects the increase of pitch-rate effects and phase lag introduced by developing separated flowfields as the mean incidence is increased.

The first harmonic components as shown in Fig. 4 are not the only terms to be considered. Because the separated flows are highly nonlinear, higher harmonic components are introduced at multiples of the first harmonic frequency. The higher harmonics become increasingly important as the amplitude is increased or as the flow becomes more dominated by separated flows. This effect is illustrated in Figs. 5 and 6 with power spectral density (psd) plots of pitching-moment and normal-force balance output for several conditions. Figure 5 shows the influence of amplitude on pitching moment for a mean incidence of 22 deg and a frequency of 2 Hz. As can be seen, for an amplitude of ± 1.75 deg, the spectrum is clearly dominated by a peak at 2 Hz. (The peaks around 40–48 Hz are due to model motion on the balance and the 50 Hz peak is due to electrical noise.) Increasing the amplitude to ± 18 deg still produces a dominant peak at 2 Hz but also at least four strong higher harmonics at 4, 6, 8, and 10 Hz.

The psd's shown in Fig. 6 are for normal-force output at a mean angle of 36 deg, where the low-amplitude motion of ± 1.75 deg is almost lost in the natural mean flow turbulence. The symbols on the plot indicate higher harmonics and show little correlation with the spectral peaks. Increasing the amplitude to ± 16 deg produces a strong peak at 2 Hz, however the second harmonic at 4 Hz is dominant. Smaller peaks also appear at 6 and 8 Hz but are not significant. It is also interesting to compare the relative size of the model response peak at about 42 Hz with the fundamental peak at 2 Hz for the two amplitudes.

The psd's discussed previously may be used to point out the limitations of harmonic analysis for these highly nonlinear flows. At $\alpha_m = 22$ deg, as shown by extensive psd analyses, the influence of amplitude at 2 Hz produces a second harmonic of about 12% of the first harmonic for $\Delta\alpha = \pm 3.5$ deg, a third harmonic of about 15% for $\Delta\alpha = 5.25$ deg and a third harmonic of about 30% for $\Delta\alpha = \pm 7$ deg. Compared with the psd's in Fig. 5, the limit of applicability of linear harmonic analysis would be an amplitude of about ± 3.5 deg or possibly ± 5.25 deg. At $\alpha = 36$ deg, an amplitude of $\pm$ 3.5 deg at 2 Hz produces a second harmonic that is about 80% of the first harmonic. As shown in Fig. 6, the first harmonic for $\Delta\alpha = 1.75$ deg at 2 Hz is almost lost in the natural turbulence at this high angle. Thus, to obtain a meaningful signal at angles close to and beyond maximum C_N, a compromise is necessary on purity of the harmonic components. Using an amplitude of ± 3.5 deg for the higher angles will be necessary because of signal-to-noise requirements, however, the presence of higher harmonics must be kept clearly in mind. For this amplitude, the higher harmonics are not a problem for mean angles of 34 deg or less. This discussion also has an impact on the higher mean angle data shown in Fig. 4.

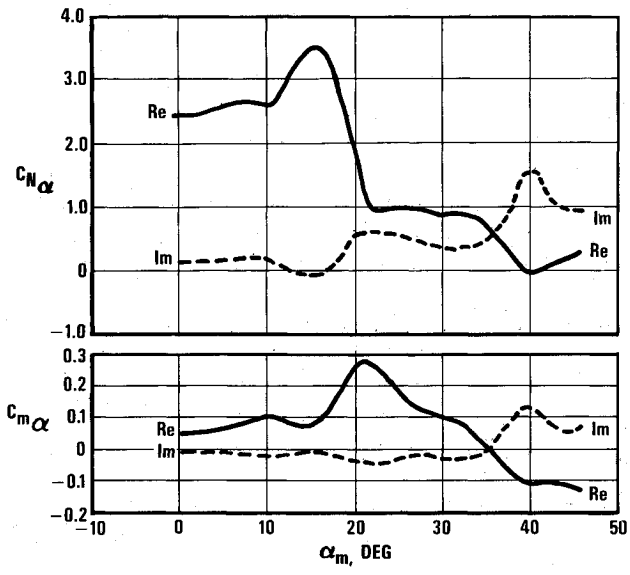

Fig. 4 Unsteady C_{N_α} and C_{m_α} vs α_m at $M = 0.22$ for $\Delta\alpha = 3.5$ deg, $f = 3$ Hz, and $k = 0.09$.

Force Data Analysis

Although limitations have just been discussed on the validity of first harmonic components for describing the forces resulting from pitch oscillations, harmonic analysis of amplitudes of ± 4 deg or less still makes sense. Since these are the types of forces that would be experienced for natural modes of vibration at their natural frequencies, such an analysis of the first harmonic is well justified. As shown in Fig. 4, the variation of C_{N_α} and C_{m_α} with mean angle is quite pronounced and would greatly impact any dynamic aeroelastic analysis.

Results are shown in Figs. 7 and 8 for the variation of C_{N_α} and C_{m_α}, respectively, with α_m and frequency. Included are the data shown in Fig. 4 for the lowest frequency of 3 Hz ($k = 0.09$). The real and imaginary parts are plotted separately to highlight the frequency effects. All data, with the exception of those for 12 Hz, were obtained with and amplitude of ± 3.5 deg. The high-frequency data at 12 Hz were obtained with a lower amplitude of 1.75-deg, as required by the high-frequency inertial load limits.

A well-known feature of the C_{N_α} data is a tendency of the imaginary data to mirror image the real data. This effect is intensified with frequency, especially beyond vortex burst. The dip for vortex flow between 10 and 18 deg for the imaginary part indicates that the increased velocities associated with well-developed vortex flows significantly reduce the pitch-rate ef-

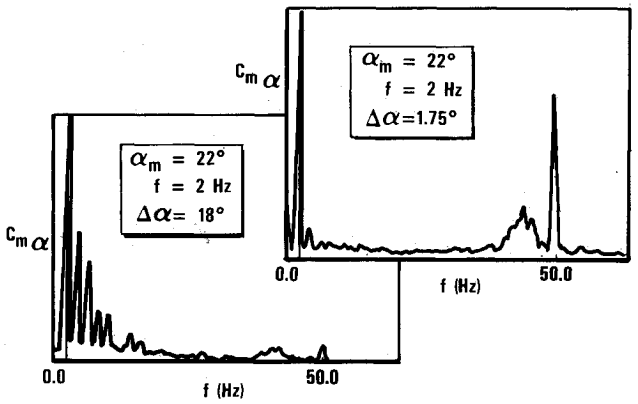

Fig. 5 Power spectral density plots for unsteady moment data to show the influence of amplitude at a lower mean angle of 22 deg.

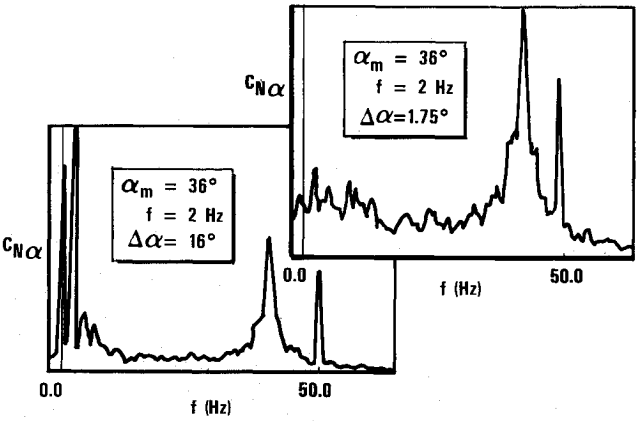

Fig. 6 Power spectral density plots for unsteady force data to show the influence of amplitude at a higher mean angle of 36 deg.

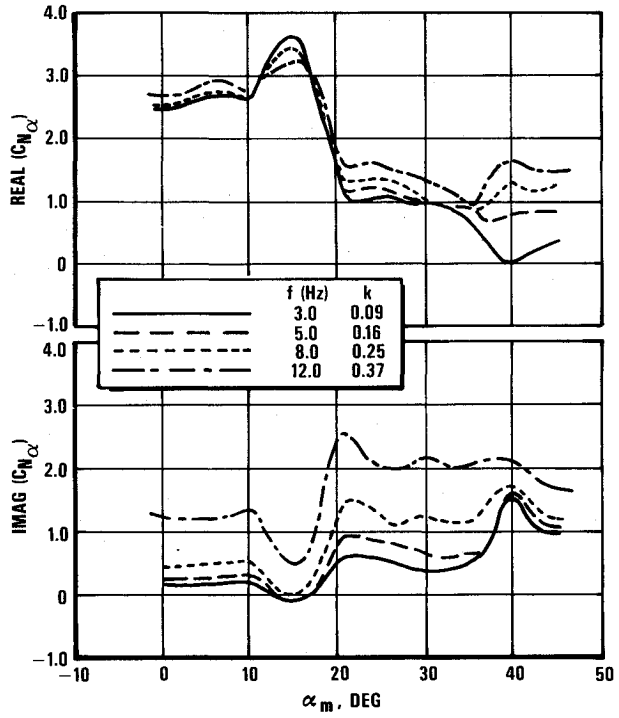

Fig. 7 Influence of mean angle and frequency on unsteady C_{N_α} from $M=0.22$ and $\Delta\alpha=1.75$–3.5 deg.

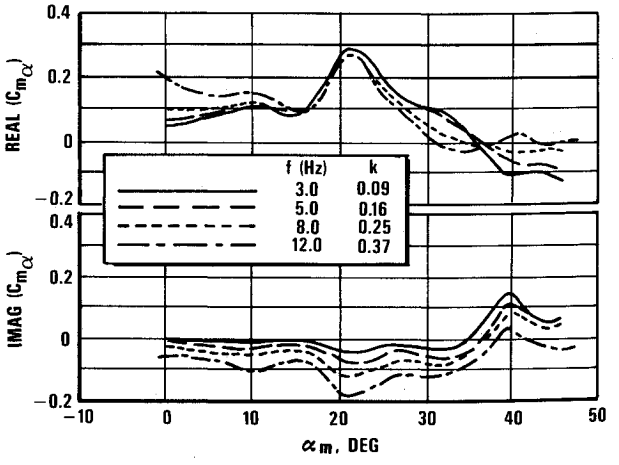

Fig. 8 Influence of mean angle and frequency on unsteady C_{m_α} from $M=0.22$ and $\Delta\alpha=1.75$–3.5 deg.

fects and phase lag of the aerodynamic response to wing motion. An increase in the imaginary part from 20 to 36 deg likewise indicates an increase in pitch-rate effects and phase lag as a result of the slower response of separated flowfields. Beyond 36 deg pitch-rate effects dominate and aerodynamic lag is more evident as shown by small increases in the imaginary part relative to the larger percentage increases in the real part.

To highlight the influence of frequency and α_m on aerodynamic lag and to distinguish this lag from pitch-rate effects, a plot of the real vs imaginary parts for C_{N_α} is shown in Fig. 9. An increase in the imaginary part is indicative of increased pitch-rate effect, which, for the low k values in these tests, tends to be nearly linear with k. Aerodynamic lag is not as clearly shown in such plots; however, in Fig. 9, it is indicated by an increase in the real part. Hence, curves that develop with increasing frequency to the right of the perpendicular through the real value at zero frequency indicate an increase in aerodynamic lag. For $\alpha_m=0$ deg, the curve develops slightly to the right of the perpendicular, indicating a nearly attached flow.

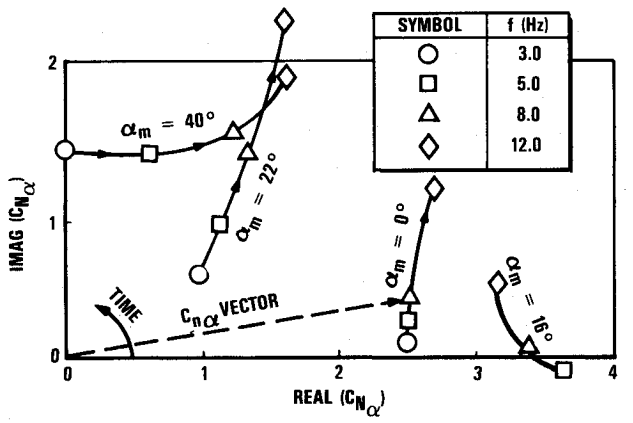

Fig. 9 Real vs imaginary parts of C_{N_α} for various frequencies and mean angles.

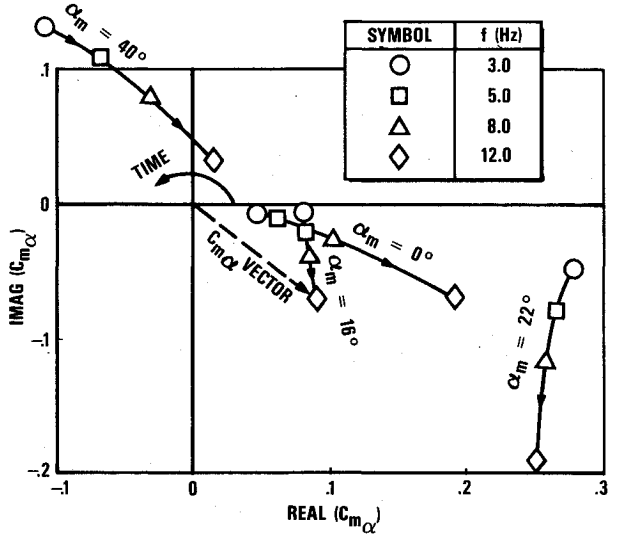

Fig. 10 Real vs imaginary parts of C_{m_α} for various frequencies and mean angles.

At the peak of vortex flow, the curve develops to the left of the perpendicular as a result of the highly organized and energetic flowfields, which produce an aerodynamic lead relative to attached linear flow.

After vortex burst at $\alpha_m=22$ deg, the vector is changed significantly with a large reduction in the real part due to the lower slope in the static data ($f=0$ Hz). There is a correspondingly large increase in the imaginary part produced by the lower velocities in the separated zones that yield an effective increase in reduced frequency. The curve development however shows a much greater departure form the perpendicular toward the right, which indicates a significant increase in aerodynamic lag as compared with $\alpha_m=0$ and 16 deg. This trend continues up to $C_{N\max}$, where the characteristics start changing, as shown in Fig. 7. After this point, the characteristics are typical of those shown in Fig. 9 for $\alpha_m=40$ deg, where the imaginary parts are almost constant within the frequency range tested, but the real parts tend to show a significant linear increase with frequency. This is because of the flowfields being much more responsive to model pitch rate and the real parts simply growing out of the imaginary parts as a result of aerodynamic lag.

Similar to the C_{N_α} data, the C_{m_α} data shown in Fig. 8 exhibit identifiable trends in the same flow regimes, i.e., attached, vortex, vortex burst, and totally separated flows. For the C_{m_α} data, a plot of the real vs imaginary parts in Fig. 10 reveals an increasing total lag with increasing frequency, as in-

dicated on all vectors rotating clockwise. This is a result of the inherent tendency of a pitching mode to produce damping that is stabilizing if the imaginary part of C_{m_α} is negative so that it opposes wing motion at maximum velocity. If the imaginary part of C_{m_α} is positive, it provides a kick to wing pitching at maximum velocity in the direction of the motion and, hence, drives the wing to increasing amplitudes of oscillation until it either structurally fails or reaches a limit amplitude. The regions of positive imaginary, C_{m_α} in Fig. 8, are thus regions of unstable aerodynamic forces for pitch oscillations. As can be seen, the stability boundary varies with both frequency and mean angle, where higher frequencies tend to reduce the unstable region. It would appear that, extrapolating from 12 Hz, a stable imaginary curve would be produced at about 16 Hz (or $k=0.5$).

The influence of amplitude on the first harmonic of C_{N_α} is shown for several α_m values in Fig. 11 for 3 Hz ($k=0.09$) and in Fig. 12 for 8 Hz ($k=0.25$). These results indicate that amplitude has a fairly small impact on all components, with the exception of the imaginary part at $\alpha_m=19$ and 36 deg for both frequencies. This is not surprising since these two angles represent major transition points, i.e., $\alpha_m=19$ deg is vortex burst and $\alpha_m=36$ deg is maximum C_N. In both cases, an increase in amplitude increases the mixture of flowfield extremes within a given cycle. More importantly, separation transition points are very sensitive to pitch rate, such that a positive pitch rate tends to delay separation and a negative pitch rate tends to delay reattachment. Since pitch rate leads wing pitch angle by 90 deg, the imaginary part is more affected by this phenomenon. Under these conditions, the higher harmonics are more significant, which reflects the highly nonlinear nature of these regions.

Pressure Data Analysis

Pressure data from the low-speed test were also analyzed on a harmonic basis. The arguments set forth previously on the presence of higher harmonics in force data are also valid for pressure data. The pressures to be discussed in this paper were measured at the four sections as shown in Fig. 1 with in situ mounted pressure transducers, which provided both steady and unsteady data. The format presents the steady mean distributions and the unsteady first harmonic distributions at the same locations. The unsteady data are shown in derivative form for real (in phase) and imaginary (out of phase) parts defined as

$$\text{Re}\,(C_p)_i = \text{Re}\,(p_i/Q\Delta\alpha)\text{per rad}$$

$$\text{Re}\,(C_p)_i = \text{Im}\,(p_i/Q\Delta\alpha)\text{per rad}$$

Where p_i is the unsteady harmonic component of pressure measured at the model oscillation frequency.

The influence of mean angle on the unsteady pressures is shown in Figs. 13–17 for $\alpha_m=10$, 19, 22.4, 36, and 42.3 deg for an amplitude of ± 3.5 deg and a frequency of 8 Hz ($k=0.25$). The general trend shown by these results is a growing importance of the imaginary part, $\text{Im}(C_p)_i$, with increasing α_m in agreement with the force data. The pressures at spanwise section 1 on the strake provide the clearest example of this effect since they are affected only by the strake vortex.

The pressures at spanwise section 2 are more complicated because they cover both the wing and strake vortices. At $\alpha_m=10$ deg, the unsteady real pressures, $\text{Re}(C_p)_i$, reflect the same shape as the steady pressures, whereas the $\text{Im}(C_p)_i$ values are almost zero. At $\alpha_m=19$ deg near vortex burst, the $\text{Re}(C_p)_i$ results are strong for the inboard part of the row associated with the strake vortex and $\text{Im}(C_p)_i$ is almost zero. The outboard part is very weak for $\text{Re}(C_p)_i$ but $\text{Im}(C_p)_i$ is about the same level, all indicating breakdown of the wing vortex. Well into burst at $\alpha_m=22.4$ deg, the trend noted at 19 deg is further developed, where the $\text{Re}(C_p)_i$ pressures associated with the wing vortex are showing a large negative lift and the $\text{Im}(C_p)_i$ are quite significant. At maximum C_N, $\alpha_m=36$ deg, both wing and strake vortices have burst at section 2, as indicated by the negative $\text{Re}(C_p)_i$ values and significant positive $\text{Im}(C_p)_i$ values. Finally, at $\alpha_m=40$ deg, the imaginary part, $\text{Im}(C_p)_i$, is dominant, as expected for totally stalled flows.

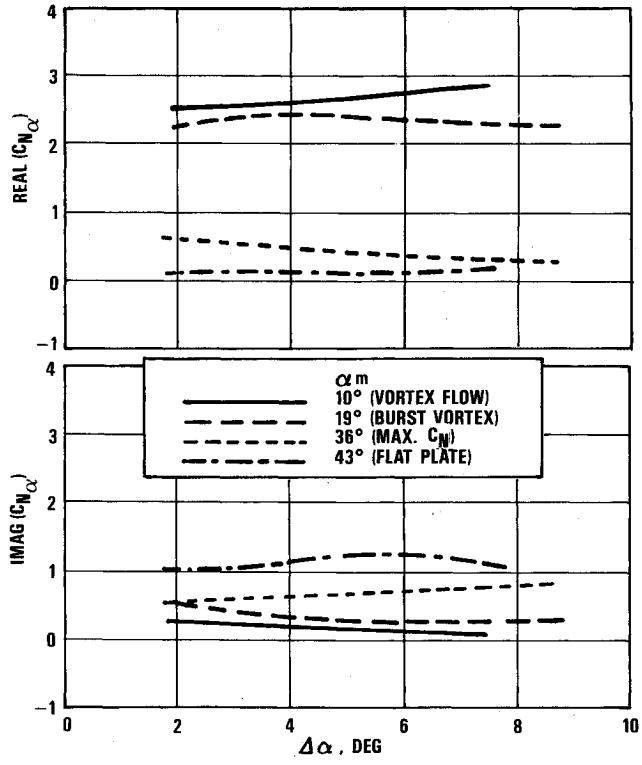

Fig. 11 Influence of oscillation amplitude on unsteady C_{N_α} for $M=0.22$ and $f=3$ Hz ($k=0.09$).

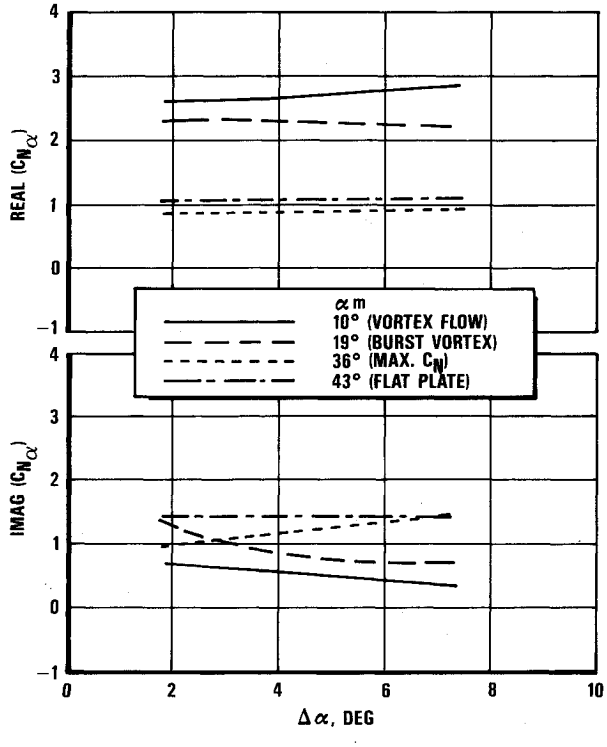

Fig. 12 Influence of oscillation amplitude on unsteady C_{N_α} for $M=0.22$ and $f=8$ Hz ($k=0.25$).

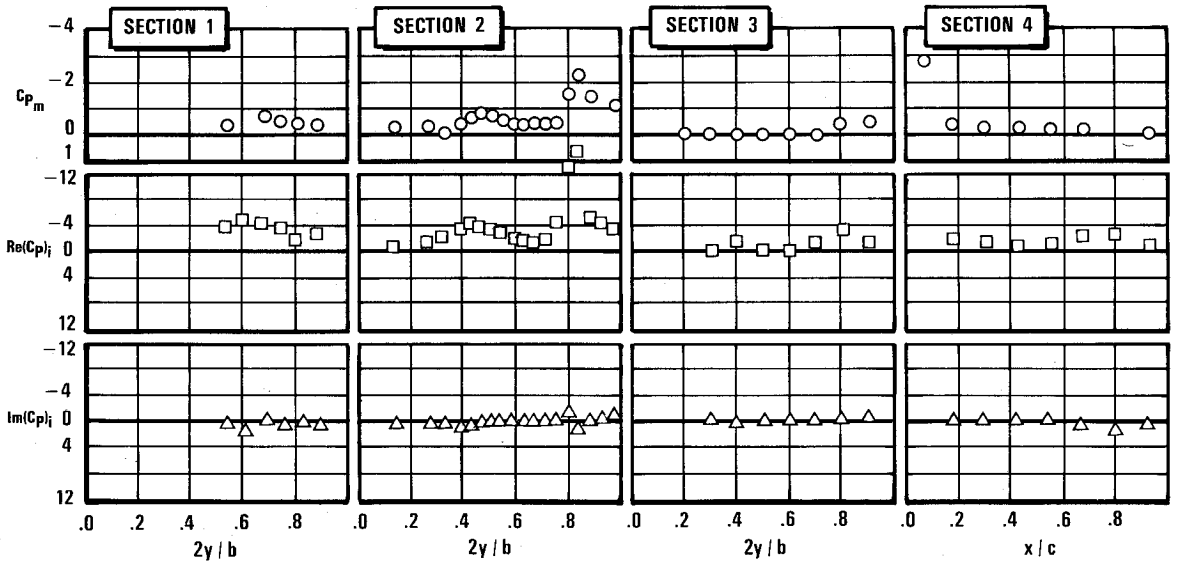

Fig. 13 Influence of mean angle on unsteady pressures at $\alpha_m = 10.01$ deg for $M = 0.22$, $\Delta\alpha = 3.64$ deg, and $f = 8$ Hz ($k = 0.25$).

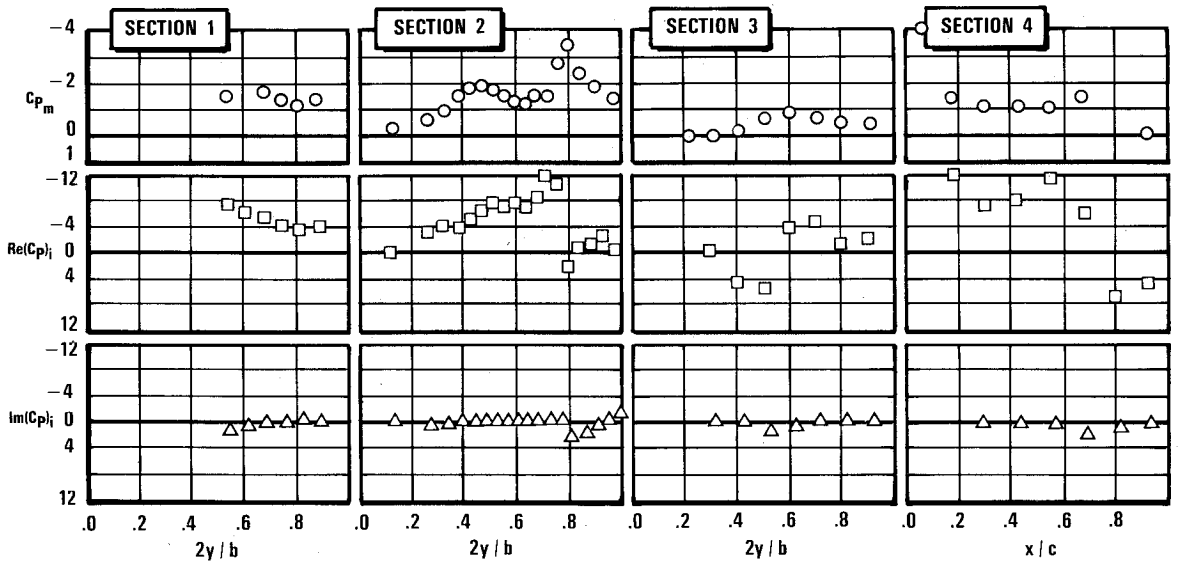

Fig. 14 Influence of mean angle on unsteady pressures at $\alpha_m = 18.96$ deg for $M = 0.22$, $\Delta\alpha = 3.47$ deg, and $f = 8$ Hz ($k = 0.25$).

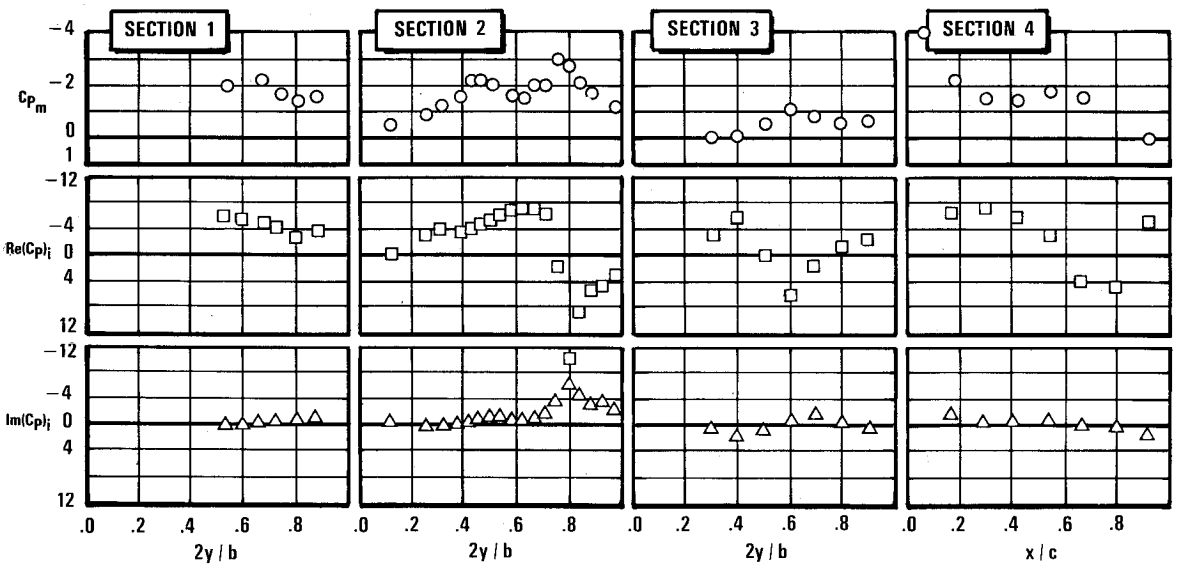

Fig. 15 Influence of mean angle on unsteady pressures at $\alpha_m = 22.44$ deg for $M = 0.22$, $\Delta\alpha = 3.45$ deg, and $f = 8$ Hz ($k = 0.25$).

At the trailing edge, spanwise section 3 is even more complicated because of the dominance of trailing-edge separation at all angles with the exception of $\alpha_m = 10$ deg. The large amplitudes at $\alpha_m = 19$ and 22.4 deg during vortex burst produce high local loadings but tend to integrate out to much smaller levels. Such loading could contribute significantly to the fatigue life of trailing-edge control surfaces and acutators.

The chordwise row at section 4 shows a streamwise cut through the region of interaction between the wing and strake vortices. This flowfield is also quite complicated, particularly during vortex bursting at $\alpha_m = 19$ and 22.4 deg, as was discussed in reference to Fig. 3. The distortion of the strake vortex into an "S" shape and consequent bursting of the combined wing and strake vortices is highly nonlinear. As a result, higher harmonics are expected to be very important for this flow regime. For the more fully separated conditions at $\alpha_m = 36$ and 42.4 deg, the flows are highly turbulent but less complicated due to their nontransient nature. It is interesting to note that the distributions at $\alpha_m = 22.4$ and 36 deg are almost mirror images of each other for the real parts.

The influence of frequency on the pressures at section 2 is shown in Fig. 18 for $\alpha_m = 22.4$ deg. The frequencies are 3, 5, 8, and 12 Hz ($k = 0.09$, 0.16, 0.25, and 0.37) and seem to have little effect on the mean pressures or the real part, $\mathrm{Re}(C_p)_i$. The influence on the imaginary part, $\mathrm{Im}(C_p)_i$, however, is far more noticeable and tends to exhibit a nearly linear increase with frequency. This is in agreement with the force data results shown in Figs. 7 and 8 for the imaginary parts.

Summarizing the overall effects of pressures, it is now evident why and how the C_N curve-slope changes occurred. At vortex burst, the increasing lift due to the strake vortex was partially negated by the loss due to the wing vortex, as shown in Figs. 14 and 15. This was also pointed out in the discussions associated with Fig. 2. The maximum value of C_N was reached when the continued building of lift by the strake vortex could no longer overcome the loss due to the wing vortex breakdown. Finally, for totally stalled flow at $\alpha_m = 42.4$ deg, the dominance of imaginary pressures likewise produced a dominance of imaginary forces. This occurrence is a natural result of the influence of pitch rate, which tends to delay separation for nose-up pitch rate and delay reattachment for a nose-down pich rate. Since maximum positive pitch rate occurs at the mean angle, the unsteady pressures tend to lead the instantaneous angle by 90 deg phase angle.

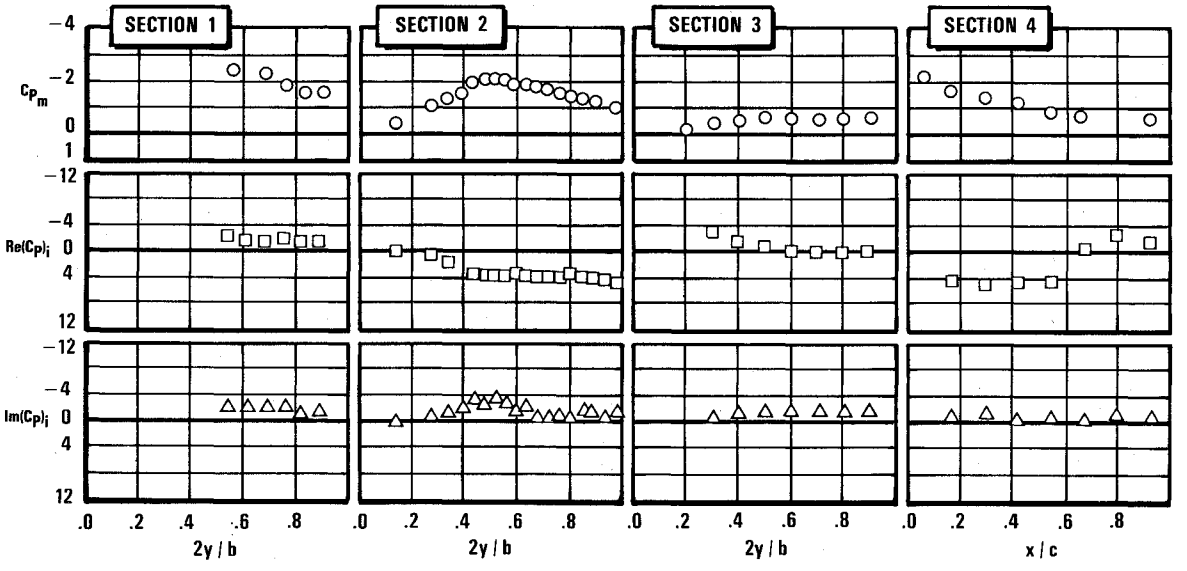

Fig. 16 Influence of mean angle on unsteady pressures at $\alpha_m = 35.84$ deg for $M = 0.22$, $\Delta\alpha = 3.38$ deg, and $f = 8$ Hz ($k = 0.25$).

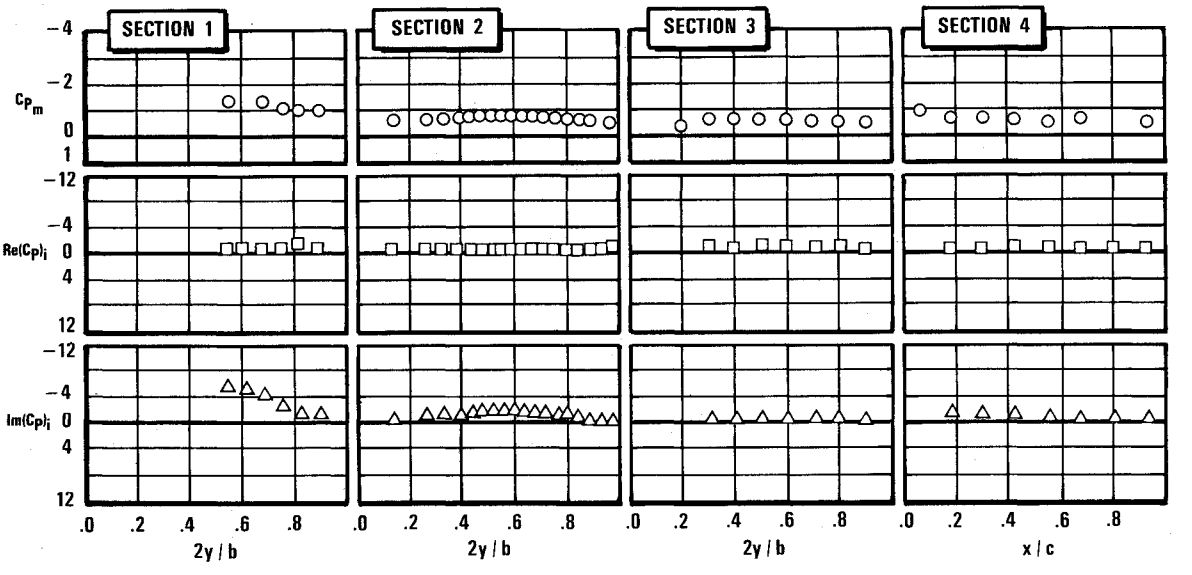

Fig. 17 Influence of mean angle on unsteady pressures at $\alpha_m = 42.29$ deg for $M = 0.22$, $\Delta\alpha = 3.54$ deg, and $f = 8$ Hz ($k = 0.25$).

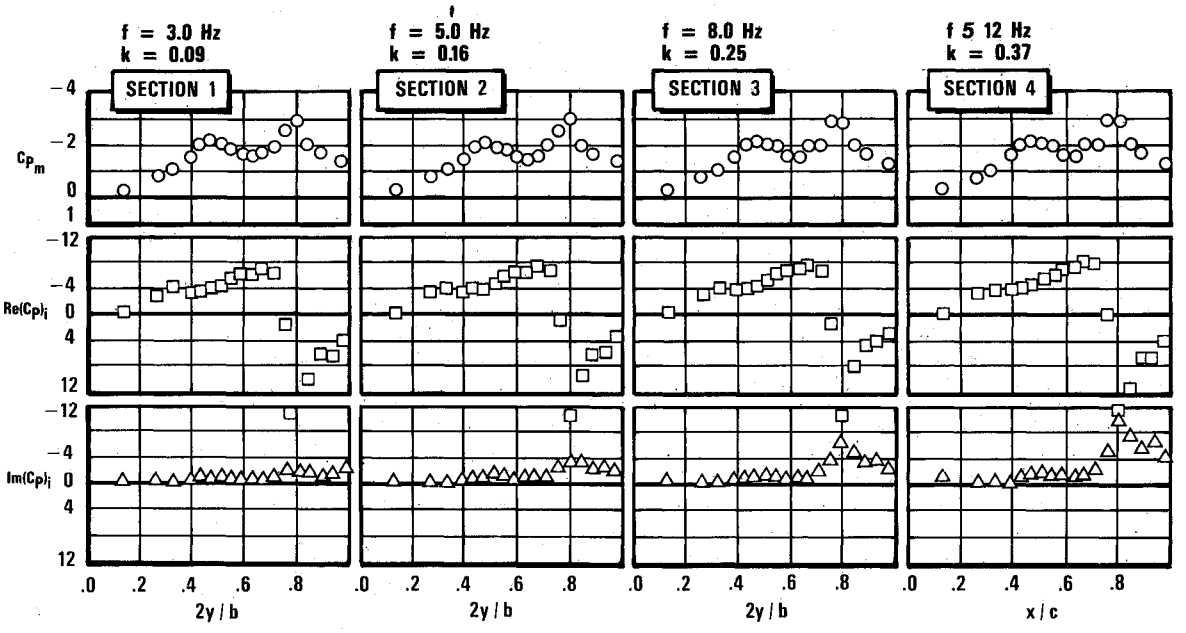

Fig. 18 Influence of frequency on the unsteady pressures at section 2 for $\alpha_m = 22.4$ deg, $M = 0.22$, and $\Delta\alpha = 1.75$–3.5 deg.

Flow-Visualization Data Analysis

Flow-visualization data were recorded from smoke flow illuminated by a chopped laser-light sheet with both a still photo camera and a video camera, as more fully described in Part I of this paper. The laser-light pulse was controlled by a device that permitted a fixed phase angle to be maintained with respect to model oscillatory motion. By varying this phase angle, it was possible to obtain a "continuous" illumination of a vortex flowfield cross section for a fixed model angle and pitch rate at different points during the cycle. The still photo camera lens was opened for a sufficient time to obtain adequate exposure: hence the photos represented multiple exposures obtained from several cycles. The video camera had sufficient sensitivity, however, to register each cycle as it was illuminated.

An example of a set of still photographs taken at pressure section 2 is shown in Fig. 19. These data were taken for the condition $\alpha_m = 22.45$ deg, $\Delta\alpha = 3.79$ deg, and $f = 1.13$ Hz ($k = 0.09$). (The velocity was 80 m/s for force and pressure testing. Hence, the frequencies were adjusted to maintain the same values of k for all testing.) The photographs show various phase angles during the cycle at 45-deg spacing. Hence, the phase angles θ and corresponding instantaneous angles of attack, $\alpha(\theta)$ deg, for Fig. 19 were as given in Table 1.

At 0 deg, the model was at the mean position with positive pitch rate; at 180 deg, it was also at the mean position but with a negative pitch rate. At 90 and 270 deg, the model was at the maximum and minimum angles, respectively.

These photographs, taken with the laser sheet located perpendicular to the model, $\alpha_m = 22.45$ deg, at pressure section 2 (65.88% of the root chord), show the positions of both the wing and strake vortices on both sides of the model. The strake vortex pair is most noticeable as the larger white areas, each with a small black center, which is the vortex core. The wing vortex pair is more difficult to see in most photographs, but is quite clear at $\theta = 180$ deg. The bright line below the left strake vortex is the intersection of the laser sheet with the model surface on the left-hand side and, thus, provides a reference for the left vortices. The right-hand side was shaded by the model center "bump"; hence, no "reference" in line was available. The "bump" also cut off the bottom of the right vortices.

Table 1 Phase angle and incidence correlations for Fig. 19

θ, deg	α (θ), deg (=22.45 deg + 3.79 deg sinθ)
0	22.45
45	25.13
90	26.24
135	25.13
180	22.45
225	19.77
270	18.66
315	19.77
369	22.45

It was possible to measure the vortex positions relative to the wing during the oscillation from these photographs. Results obtained from measuring Fig. 19 are shown in Fig. 20 for all four vortices. The spanwise location is shown as a local semispan fraction, and the vertical position is also shown normalized by the local semispan. The mean vortex core locations on the right-hand side agree very well with the steady mean pressure peak positions shown in Fig. 18 for $k = 0.09$. The locations are 0.46 and 0.80 for the strake and wing vortices, respectively, in both Figs. 18 and 20.

Also shown in Fig. 20 are the directions of core motions as denoted by both the arrows and phase angle. The right vortices show a counterclockwise rotation, and the left vortices show the expected clockwise motion for the strake vortex but counterclockwise for the wing vortex. The principal motion for all vortices, however, is vertical.

Two very important conclusions can be drawn from these results. First, it is clear from Fig. 19 that neither the wing nor strake vortices burst at section 2 during the oscillation at $\alpha_m = 22.45$ deg. Thus, the loss in suction shown by the wing vortex in Figs. 15 and 18 is not because of bursting at pressure section 2. Second, it appears that the loss in suction from the wing vortex is instead due to the motion of that vortex away from the wing. Since the suction force produced by a vortex is inversely proportional to the square of the distance perpendicular to the vortex core, a greater separation between the wing and vortex will result in lower surface suction on the wing. As shown in Fig. 20, the wing vortex vertical position varies from 0.12 to 0.17, which, for a constant vortex strength, produces a relative variation of surface suction from 1.0 at the minimum position ($\theta = 270$ deg) to about 0.5 at the maximum position ($\theta = 90$ deg). This extreme is not shown by the strake vortex, whose vertical position varies only from 0.22 to 0.25 during the cycle.

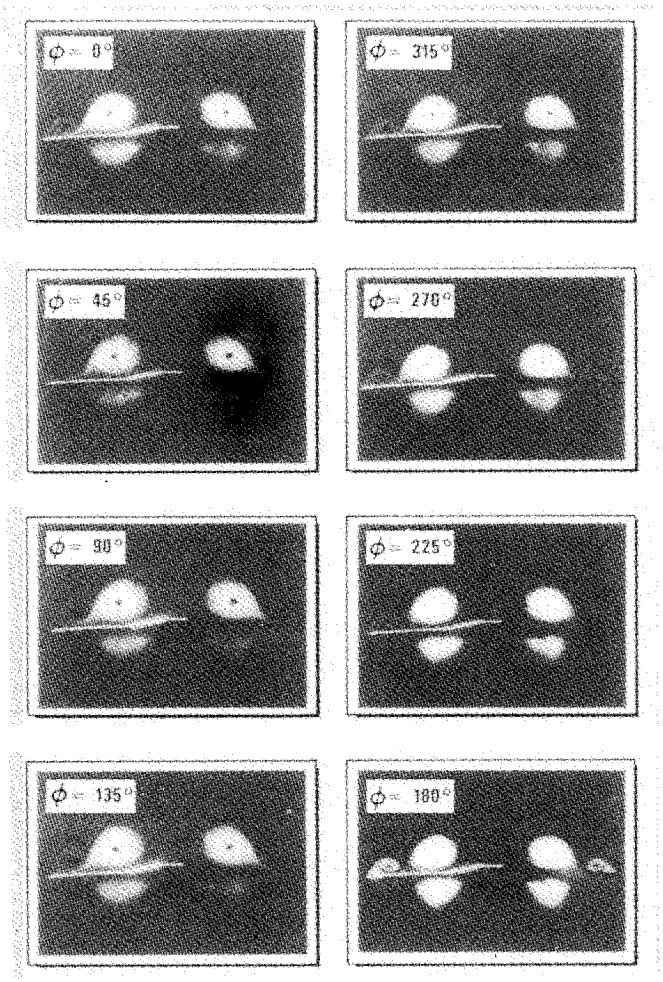

Fig. 19 Unsteady vortex flow visualization at section 2 for $\alpha_m = 22.45$ deg.

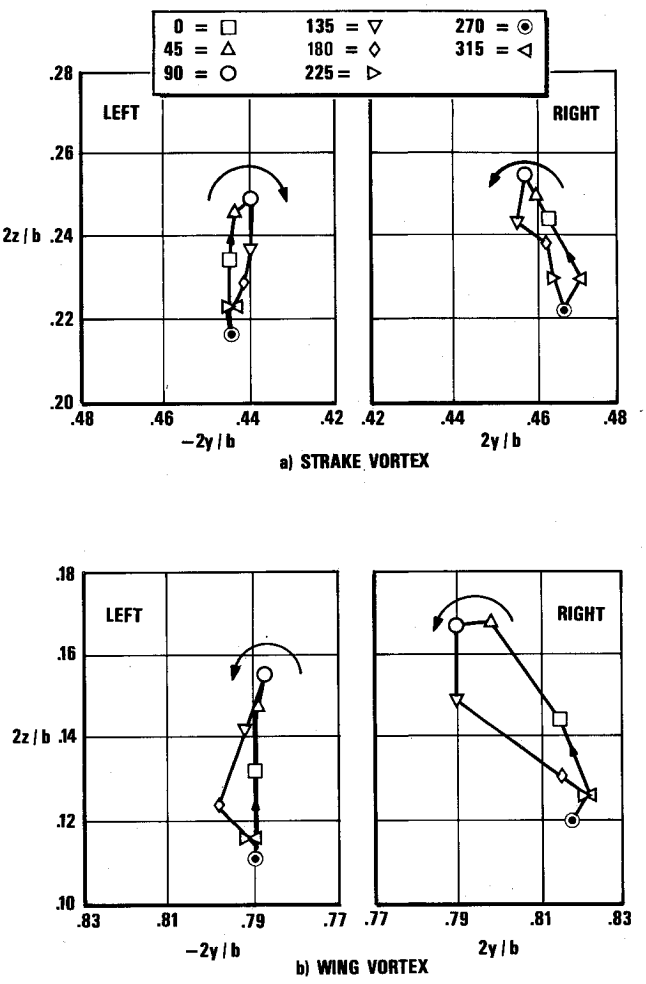

Fig. 20 Unsteady vortex positions at section 2 for $\alpha_m = 22.45$ deg, $\Delta\alpha = 3.79$ deg, and $f = 1.18$ Hz ($k = 0.09$) (measured from Fig. 19).

Flow-visualization data similar to those shown in Figs. 19 and 20 are available for this test from other mean angles, amplitudes, and frequencies. As demonstrated by the preceding analysis, these data provide invaluable insight when combined with both pressure and force data, to the phenomena involved in the flowfields and how they react with the model to produce the aerodynamic forces.

Conclusions

A discussion has been presented on the steady and unsteady aerodynamic forces that were developed on the straked wing model oscillating in pitch as described in Part I of this paper. The mean angle of attack ranged from −8 to 50 deg with amplitudes limited to a maximum of ±8 deg and frequencies up to 12 Hz herein. The data analyzed included forces, pressures, and flow-visualization results for the steady mean values and the first harmonic unsteady values.

The important flow regimes were identified as linear, vortex, burst vortex, and totally separated flows. The unsteady harmonic normal-force data tracked the steady-force data for the real (in phase) part and the imaginary part exhibited an increasing aerodynamic lag tendency at higher angles and frequencies. The unsteady harmonic pitching-moment data also showed similar characteristics with an unstable region defined above maximum C_N that diminished with increasing frequencies.

The influence of mean angle on unsteady data was found to be very significant. Besides influencing the phase angle, amplitude changes ranged up to about a 60% reduction in C_{N_α} when compared with values at the low-angle attached-flow data. Thus, aeroelastic analyses concerned with flutter and dynamic response would be impacted greatly when considering the high-angle separated-flow regimes.

Harmonic analysis of the pressure data was used to improve the understanding of how the trends in force data occurred. It was possible to separate the impact of wing vortex bursting and strake vortex bursting on developing normal force with increasing angle up to and beyond the maximum value of C_N. Beyond this point the almost purely imaginary values of C_{N_α} were shown to be a result of the dominance of imaginary pressures and very small real pressure levels. This dominance was because of the tendency of fully separated flows to be more sensitive to pitch rate rather than incidence change.

Flow-visualization data analysis provided further information on the flow structure during vortex bursting at $\alpha_m = 22.45$ deg. It was shown that pressure changes produced at section 2 were not a result of wing vortex bursting at that point, but were probably due to vortex vertical displacement caused by downstream bursting.

Finally, it must be concluded that this paper has demonstrated the value of combining force, pressure, and flow-visualization results as an approach to understanding the highly complicated flowfields incurred during this test.

Acknowledgments

The test program discussed in this paper was funded under contract F33615-85-C-3013 through the Flight Dynamics Laboratory of the Air Force Wright Aeronautical Laboratories.

Analysis and data reduction were accomplished under a cooperative effort between General Dynamics and the NLR.

References

[1]Herbst, W. B., "Dynamics of Air Combat," *Journal of Aircraft*, Vol. 20, July 1983, pp. 594–598.

[2]Lang, J. and Francis, M. S., "Unsteady Aerodynamics and Dynamic Aircraft Maneuverability," Paper 29, presented at the AGARD Symposium on Unsteady Aerodynamics—Fundamentals and Applications to Aircraft Dynamics, AGARD CP 386, May 1985.

[3]Cunningham, A. M., Jr., "Vortex Flow Hysteresis," Paper 11, NASA CP 2416, Vol. I, 1986.

[4]Cunningham, A. M., Jr. and Benepe, D. B., Sr., "Prediction of Transonic Aircraft Buffet Response," Paper 3, AGARD CP-226, 1977.

[5]Cunningham, A. M. Jr., et al, *Unsteady Low-Speed Wind Tunnel Test of a Straked Delta Wing, Oscillating in Pitch*, AFWAL-TR-87-3098, Parts I–VI, April 1988.

[6]Malcolm, G. N., "Impact of High-Alpha Aerodynamics on Dynamic Stability Parameters of Aircraft and Missiles," Paper 2, AGARD-LS-114, 1981.